Research on Engineering Structures & Materials
www.jresm.org
Research Group

Research Article

Frequency-dependent effects of CFRP retrofitting on the equivalent viscous damping ratio of RC frames

Antoine Azar [*,a], Kamal Safa [b], Fouad Kaddah [c]

Dept. of Civil Eng., the Higher School of Engineering ESIB, Saint Joseph University of Beirut, Lebanon

Article Info

Article History:

Received 23 Nov 2025

Accepted 25 Mar 2026

Keywords:

Carbon fiber-reinforced polymer;
Equivalent viscous damping ratio;
Hinge relocation;
Cyclic endurance

Abstract

Conventional seismic assessment of reinforced concrete (RC) frames retrofitted with externally bonded carbon fiber–reinforced polymer (CFRP) typically relies on quasi-static force–deformation metrics, overlooking the frequency-dependent evolution of energy dissipation. This study investigates the effects of excitation frequency and CFRP detailing system on the dynamic response of retrofitted frames using an energy-based framework and the equivalent viscous damping ratio (EVDR). A three-story RC frame was subjected to harmonic base displacement over a range of frequencies and evaluated using two CFRP retrofit configurations at beam plastic hinges: an extended flange-bonded CFRP sheet configuration and a configuration designed to promote plastic hinge relocation. Results show that, at resonance, the extended flange configuration increased elastic energy by 67% and reduced hysteretic damping by 40%, leading to excessive force amplification that compromised cyclic endurance. In contrast, the hinge relocation configuration limited elastic energy growth to 30%, maintained higher hysteretic damping, and improved cyclic endurance. Moreover, CFRP retrofitting was most effective below resonance and became progressively less effective at higher excitation frequencies. These findings underscore that effective CFRP retrofit design must jointly consider the targeted excitation frequency and CFRP detailing system to optimize energy dissipation and structural resilience.

1. Introduction

Fiber-reinforced polymer composites, when externally bonded to RC members, have become a widely used technique for seismic strengthening due to their high strength-to-weight ratio, corrosion resistance, and ease of installation [1]. Over the past two decades, experimental and analytical investigations have shown that properly detailed FRP retrofitting can significantly enhance the strength and deformation capacity of RC beam–column joints [2–4]. These advances have motivated the development of design guidelines and supported broader implementation of FRP retrofit systems to upgrade aging, seismically vulnerable RC structures [1,5,6].

A key mechanism by which FRP retrofitting improves the behavior of RC frames is the strategic relocation of plastic hinges away from column faces and joint cores toward the beam span. This relocation reduces inelastic demand on joint regions and promotes a ductile response characterized by a strong-column/weak-beam mechanism, thereby shifting the global failure pattern toward a controlled beam-hinging mode.

The concept of plastic hinge relocation has been extensively explored in structural retrofitting research, with two mains externally bonded FRP retrofit schemes reported in the literature: web-bonded and flange-bonded configurations. Both techniques have demonstrated the ability to enhance joint performance and shift inelastic deformations into the beam span [2,4,7,9]. However,

*Corresponding author: antoine.azar@net.usj.edu.lb
[a]orcid.org/0000-0002-7557-5971; [b]orcid.org/0009-0003-9111-0132; [c]orcid.org/0000-0003-0015-6390
DOI: http://dx.doi.org/10.17515/resm2026-1360ma1123rs

the web-bonded approach imposes significant practical limitations in three-dimensional framing systems. Slabs and transverse beams obstruct access to the beam webs and joint faces, rendering this method largely infeasible for widespread field implementation [2]. In contrast, flange-bonded techniques address these access constraints by reinforcing the top and bottom beam flange surfaces, which remain accessible even in the presence of floor systems. A comparative analysis by Zarandi et al. [2] further showed that flange-bonded configurations can achieve hinge relocation and ductility enhancement comparable to those of web-bonded systems, while requiring less FRP material, thereby reducing retrofit costs and increasing feasibility for field implementation.

Regardless of whether a web-bonded or flange-bonded configuration is adopted, effective plastic hinge relocation using externally bonded FRP is governed primarily by two design variables: CFRP ply count (thickness) and the CFRP development length L_f, defined as the distance from the column face along the beam to the laminate termination (cut-off). Experimental and numerical studies have consistently shown that these parameters control the ability to relocate plastic hinging into the beam span. Mahini and Ronagh [7], through a systematic investigation of web-bonded layouts, demonstrated that adequate ply count and development length are indispensable for successful hinge relocation and the restoration of joint integrity. They further reported that insufficient CFRP thickness can concentrate damage at the joint interface and may not yield meaningful improvements in joint ductility.

For flange-bonded systems, Arowojolu et al. [4] conducted monotonic pushover and cyclic tests on deficient exterior beam–column joints, systematically varying the CFRP development length from approximately two-thirds to one time the beam depth ($L_f \approx 0.67h_b$–$1h_b$, where h_b is the beam depth) and adjusting ply thickness to assess hinge relocation. They reported that increasing L_f from $0.67h_b$ to $1h_b$ produced no appreciable gain in load capacity but resulted in slightly increased joint cracking. They suggested an optimal L_f of approximately two-thirds the beam depth for successful hinge relocation, shorter than the conventional $1h_b$ length recommended by Paulay and Priestley [8].

Complementing this work, Hejazi et al. [9] conducted parametric pushover analyses of interior joints with moderate ductility, adopting the development length proposed by Paulay and Priestley [8] and varying the number of flange-bonded plies. They concluded that a five-layer configuration was the most cost-effective option for successful plastic hinge relocation, as applying further layers provided no additional benefit to the relocation mechanism. Furthermore, they recommended selecting the ply count based on the shear and moment demands imposed on the intersecting beam and column members at the joint.

Another critical requirement for reliable FRP retrofitting is robust anchorage of externally bonded sheets to ensure effective engagement of the FRP reinforcement under seismic loading. Without special anchorage, premature debonding may occur before the FRP approaches its tensile capacity, thereby limiting the effectiveness of the retrofit. Accordingly, prior studies have proposed and validated several anchorage systems, such as FRP wraps and steel fasteners, to delay or prevent debonding [3,13,21]. In cyclic tests on shear-critical RC beam–column joints investigated by Antonopoulos and Triantafillou [3], specimens retrofitted with externally bonded FRP and provided with anchorage systems achieved significantly higher shear strength, energy dissipation capacity, and stiffness than their unanchored counterparts. Similarly, Sakr et al. [13] reported premature debonding in several CFRP-retrofitted exterior beam–column joints tested under cyclic loading. To overcome this limitation, they further investigated a mechanically fastened alternative using steel plates and anchors. Their results indicated that such fasteners substantially enhanced the ultimate joint capacity while promoting a ductile beam-hinging response.

Despite extensive component-level validation, comparatively few studies have examined the efficacy of FRP retrofit at the whole-frame system scale, where interactions among retrofitted members and damage redistribution govern the overall response. Wang et al. [14] demonstrated through pseudo-static cyclic testing of previously damaged RC frames retrofitted with externally bonded CFRP that retrofitting not only restores lateral strength, stiffness, and ductility but can also yield performance metrics that exceed those of the original, undamaged frames. Comparable system-level enhancements have been observed in additional full-scale frame studies [2,12,15-20].

Another important metric is the seismic performance level achieved after retrofitting, as defined by performance-based design guidelines [10,11,21]. In this context, Zarandi et al. [2] evaluated and compared the system-level seismic response of an original RC frame and its retrofitted counterparts employing flange-bonded and web-bonded FRP schemes. Capacity curves obtained from nonlinear pushover analysis were integrated into a capacity–demand procedure [11] to determine the performance point and the associated performance level for each frame. Their results showed that, under an earthquake demand corresponding to a design base acceleration of 0.25g, the original frame failed to satisfy the Life Safety (LS) requirement, whereas both FRP-retrofitted frames met this criterion. However, a direct comparison of the capacity curves showed that the flange-bonded scheme significantly outperformed the web-bonded counterpart, improving not only the frame's global strength and ductility but also its overall seismic performance. This superiority was further highlighted at a higher seismic demand of 0.30g, where the flange-bonded configuration continued to satisfy the LS requirement, whereas the web-bonded scheme no longer met this criterion.

However, the vast majority of prior studies have relied on quasi-static cyclic or monotonic loading to assess retrofit effectiveness, focusing primarily on force–deformation metrics. A key research gap remains in understanding the frequency-dependent dynamic behavior of CFRP-retrofitted RC frames, specifically how energy dissipation and damping characteristics evolve under harmonic or broadband frequency excitations that include the structure's fundamental frequency. The effect of excitation frequency is critical, as earthquake ground motions can induce pronounced response amplification when their dominant spectral components approach a structure's natural frequencies, leading to resonance. In such scenarios, the structural response is governed by the combined influence of excitation amplitude and resonance effect, which in turn can cause excessive stiffness degradation, energy dissipation, and cumulative damage. Moreover, prior research has shown that CFRP retrofitting can modify the structure's hysteretic behavior and stiffness evolution [14-16]. This, in turn, can change the partitioning of input energy among recoverable strain energy, damping-related dissipation, and damage-associated mechanisms. Therefore, explicit consideration of excitation-frequency effects is essential for reliable performance-based seismic assessment of CFRP-retrofitted RC frames.

The primary objective of this study is to assess how excitation frequency and CFRP retrofit detailing system influence the energy dissipation and damping characteristics of retrofitted RC frames. By systematically varying the excitation frequency relative to the structure's fundamental frequency and comparing different retrofit configurations, the study establishes a unified framework that links excitation frequency, retrofit detailing, and dynamic energy dissipation, thereby addressing a critical gap in the system-level assessment of CFRP-retrofitted RC frames.

2. Numerical Investigation

2.1. Description of Test Structures: Primary and CFRP-Retrofitted Frames

To evaluate the effect of CFRP retrofitting on the seismic performance of reinforced concrete frames, a numerical simulation was carried out using Abaqus/CAE [22] on a three-story, single-bay, moment-resisting RC frame. The model, characterized by uniform cross-sectional dimensions for all beams and columns across all stories, was developed without CFRP retrofitting and is referred to as the primary frame. It served as the baseline for assessing the dynamic response and energy-dissipation characteristics under sinusoidal base excitation across a range of frequencies.

For comparative analysis, two additional models, exact replicas of the primary frame, were developed with externally bonded CFRP sheets applied at the anticipated plastic hinge regions. These models employed two distinct retrofit configurations, designated as Configuration A and Configuration B, allowing for a systematic comparison of energy dissipation behavior between the primary and retrofitted frames under identical base displacement histories (Fig. 1). Both configurations utilized CFRP composites but differed in retrofit strategy, ply thickness, and development length, as summarized in Table 1.

Table 1. CFRP retrofit configurations: Mechanical and geometric properties

Configuration	Location	CFRP System	Fiber Orientation	No. of Layers	E_f (GPa)	ε_{fu} %	Total thickness (mm)	L_f
A	Column wrapping	UD fabric	$[45°/-45°]_2$	4	133.86	1.36	1	$2h_c$
	Beam flanges	HM laminate	0°	3	165	1.87	3	$2h_b$
B	Column wrapping	UD fabric	$[45°/-45°]_2$	4	133.86	1.36	1	$2h_c$
	Joint core/beam webs	HM laminate (U-shaped)	0°	1	165	1.87	1	$0.67h_b$ (from beam-column interface)
	Beam flanges	HM laminate	0°	3	165	1.87	3	$0.67h_b$

UD = unidirectional; HM = high modulus; E_f = elastic modulus; ε_{fu} = ultimate tensile strain

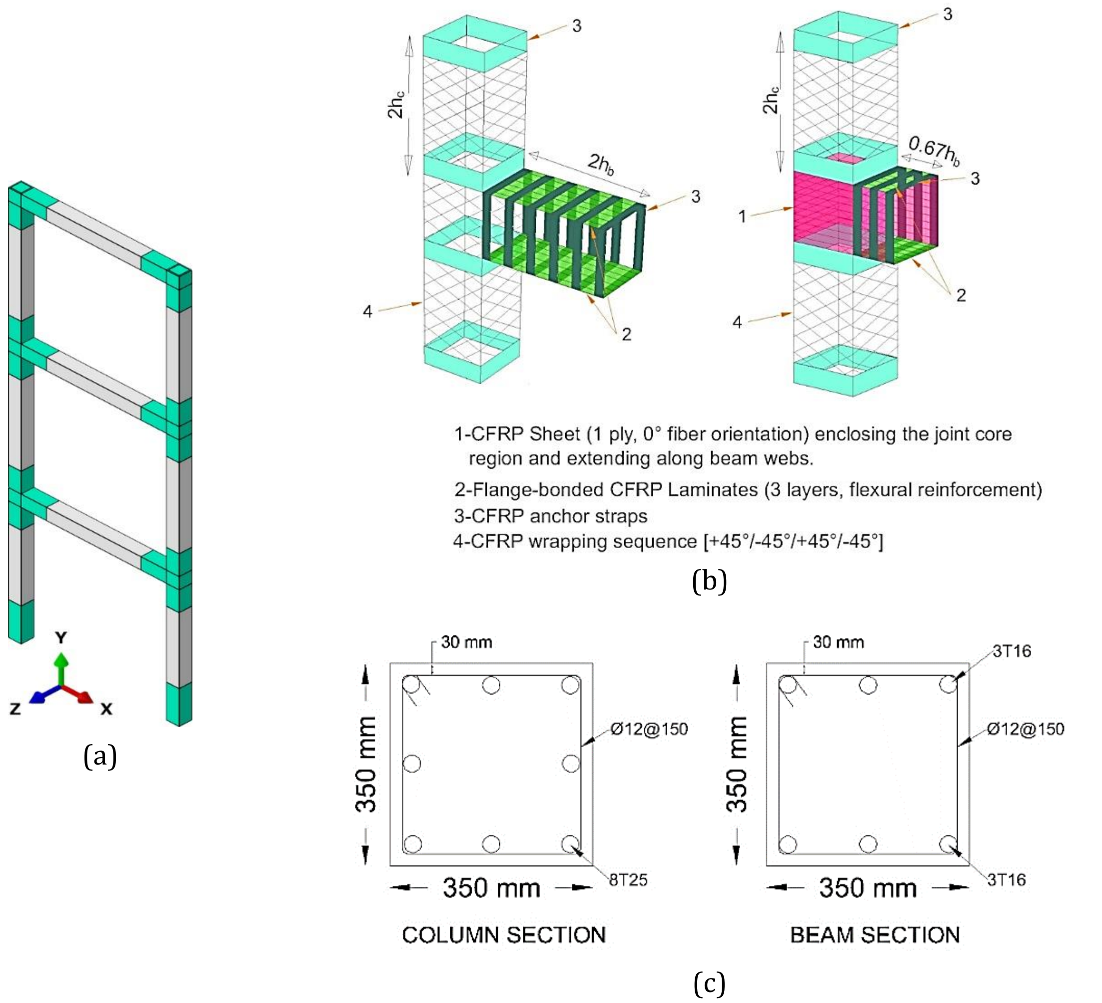

Fig. 1. Integration of CFRP retrofitting into the moment-resisting RC frame: (a) 3D model of the three-story RC frame; (b) details of CFRP application at beam and column joints for Configurations A and B; (c) cross-sectional details of beam and column members

Configuration A employed a two-stage CFRP retrofit scheme. In the first stage, the column plastic hinge regions were wrapped with four plies of unidirectional CFRP sheets arranged in an alternating stacking sequence, extending a distance of $2h_c$ (where h_c is the column depth) above and below the beam–column interface to enhance shear resistance. In the second stage, flexural retrofit was provided by bonding high-modulus CFRP laminates to both beam flanges, with fibers oriented longitudinally. The laminate development length, $L_f = 2h_b$ (where h_b is the beam depth), measured from the column face, was selected in accordance with ACI 440.2R-17 [1].

Configuration B employed a three-stage CFRP retrofit scheme specifically designed to relocate the plastic hinge away from the beam-column interface. In the first stage, column plastic hinge zones were wrapped with four plies of unidirectional CFRP in an alternating [45°/−45°/45°/−45°] lay-up (relative to the longitudinal axis), similar to Configuration A. In the second stage, high-modulus CFRP laminates were bonded to the beam flanges (top and bottom faces), with fibers oriented longitudinally. A reduced development length of $L_f = 0.67h_b$, measured from the column face, was adopted in accordance with Arowojolu et al. [4], who demonstrated that plastic hinge relocation can be effectively achieved at both $0.67h_b$ and $1h_b$, with the shorter extension minimizing joint-core damage while preserving comparable flexural capacity.

In the third stage, a single-ply U-shaped CFRP laminate (nominal thickness ≈ 1.0 mm) was applied over the joint core and adjacent beam web regions. The fibers were aligned with the beam axis (0° orientation), and the wrap terminated at the same development length as the flange-bonded laminates. This web-bonded detailing has been shown to effectively shift plastic hinge formation away from the beam–column interface toward the CFRP termination region [7]. All CFRP configurations were anchored using strap systems placed at strategic locations to prevent end-peeling failures and ensure effective transfer of tensile forces, thereby enabling full development of the CFRP strengthening capacity, as illustrated in Fig. 1(b).

2.2. Numerical Simulation Investigation

Modal analysis was initially performed on the primary frame and the two CFRP-retrofitted frame configurations, A and B, to extract their fundamental vibration modes and associated natural frequencies. Based on these frequencies, the Rayleigh damping coefficients, α (mass-proportional) and β (stiffness-proportional), were then determined for a prescribed material damping ratio of 5%. Subsequently, the calculated damping parameters were incorporated into each model prior to conducting the nonlinear dynamic simulations.

Each finite element model was then subjected to a one-second static gravity preload to incorporate self-weight effects into the global mass matrix. Following this, Incremental Dynamic Analysis (IDA) was initiated. The primary frame was subjected to a sinusoidal base excitation $u(t) = A \sin(\omega t)$ at the corresponding resonance frequency, where A denotes the displacement amplitude (mm), ω is the circular frequency (rad/s) associated with the fundamental natural mode of the structure, and t is the time variable (s). The amplitude A was calibrated so that the primary frame reached its threshold limit after 14 consecutive loading cycles. The IDA simulation was terminated once any cross-section reached its ultimate curvature φ_u, defined as the earliest occurrence of one of two local failure modes outlined by Valles [23]:

- Crushing of concrete at the extreme compression fiber
- Reaching the ultimate tensile strain of longitudinal steel reinforcement

Following amplitude calibration of the primary frame, the same base excitation was applied to both CFRP-retrofitted configurations to enable direct comparison of energy dissipation and structural response. The evaluation criteria and limit-state definitions established for the primary frame were consistently maintained for the retrofitted configurations. Throughout the analysis, CFRP strain was continuously monitored, with failure defined as the point at which the composite material reached its ultimate tensile strain, as specified in Table 1.

It is worth noting that throughout all conducted dynamic analyses, the governing limit state corresponded to the attainment of the ultimate curvature in the beam plastic hinge region, consistently occurring in the beam segment rather than in the column elements across all frames. No premature column yielding, global instability, or CFRP rupture was observed before reaching this curvature threshold, indicating that the beam flexural capacity controlled the structural response under the applied cyclic loading protocol. Steel reinforcement failure was assumed to occur at a tensile strain of 5%, in accordance with the maximum usable strain limit for longitudinal bars as specified in FEMA 356 [10], beyond which rebar fracture is expected.

Three primary energy components were extracted and quantified from Abaqus history output across loading cycles: cumulative viscous dissipated energy (E_v), cumulative plastic (hysteretic) dissipated energy (E_p), and maximum recoverable elastic strain energy per cycle (E_{se}). These quantities were used to compute equivalent viscous damping ratios, decomposed into viscous ($\xi_{viscous}$) and hysteretic (ξ_{hyst}) components to enable systematic comparison between the primary frame and the CFRP-retrofitted frames. The investigation was complemented by off-resonance analyses at ±25% of the fundamental frequency, during which energetic response and EVDR trends were evaluated and compared with the baseline resonant behavior.

3. Theoretical Considerations: Energy Balance Principles and Strain Energy Method

3.1. Energy Balance Under Harmonic Excitation

As outlined in Chopra's work on structural dynamics [24], the energy response terms for a single-degree-of-freedom (SDOF) system subjected to earthquake ground motion can be derived from the equation of motion, expressed as follows:

$$E_k + E_v + E_I = E_{input} \tag{1}$$

where E_k represents the kinetic energy, and E_I denotes the internal energy, which comprises the recoverable elastic strain energy and the cumulative hysteretic energy (E_{hyst}) resulting from inelastic deformation. The latter includes both E_p and damage-related energy dissipation (E_D). E_{input} corresponds to the total input energy imparted to the system by the ground motion.

In the present study, hysteretic losses arise almost entirely from plastic deformation; damage-related dissipation contributes only a negligible share. Consequently, E_{hyst} will be treated as equivalent to the plastic dissipated energy for all subsequent analyses.

3.2. Evaluation of the EVDR Using the Strain Energy Method

The strain energy method calculates the EVDR as the ratio of dissipated energy to the elastic strain energy at the maximum force and displacement per hysteretic loop (Fig. 2). Initially developed for linear-elastic systems, Jacobsen extended it to accommodate nonlinear behavior [25-27]. In nonlinear systems, it is crucial to distinguish between the equivalent viscous damping component ($\xi_{viscous}$), which is frequency-dependent (Eq. (2)), and the equivalent hysteretic damping component (ξ_{hyst}), which arises from frequency-independent plastic dissipation (Eq. (3)) [28]. Both components are evaluated on a cycle-by-cycle basis.

$$\xi_{viscous} = \frac{E_{v,cyc}}{2\pi E_{se}}\left(\frac{\omega_n}{\omega}\right) \tag{2}$$

$$\xi_{hyst} = \frac{E_{hyst,cyc}}{2\pi E_{se}} \tag{3}$$

$$\xi_{eq,total} = \xi_{viscous} + \xi_{hyst} \tag{4}$$

where ω_n and ω are the natural and excitation angular frequencies, respectively; $E_{v,cyc}$, and $E_{hyst,cyc}$ are the viscous and hysteretic dissipated energy per cycle. In this study, Abaqus directly extracts these energy components through history output requests, as previously mentioned, eliminating the need to compute Jacobsen's areas from hysteretic loops.

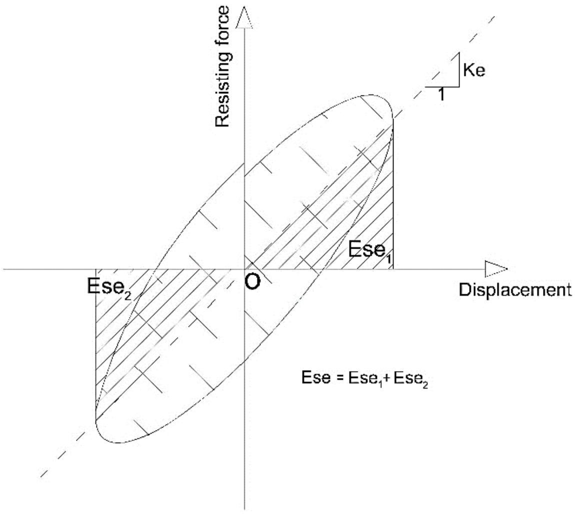

Fig. 2. Hysteresis loop illustrating energy dissipation and absorption

3.3. Takeda Degrading Model

A principal methodological contribution of this study is the explicit integration of stiffness degradation into the cycle-by-cycle evaluation of the EVDR. In conventional equivalent viscous damping formulations, $\xi_{viscous}$ is typically assumed constant (often 5%), implicitly treating it as independent of stiffness degradation during inelastic cyclic loading [29-31]. Likewise, nonlinear time-history analyses frequently model viscous dissipation using the initial stiffness. However, because the damping force depends on both the adopted stiffness and the response velocity, retaining the initial stiffness after structural yielding can generate spurious damping forces, as demonstrated by Priestley et al. [31]. Accordingly, using the tangent (degraded) stiffness as the basis for $\xi_{viscous}$ calculations provides a more physically transparent and consistent representation of damping in degrading RC frames [29,30].

The present study incorporates a Takeda degrading hysteresis model directly into the equivalent damping evaluation by updating the degraded stiffness and, consequently, the corresponding ω_n at each loading cycle. The viscous component of the EVDR is then evaluated for each cycle using Eq. (2), enabling $\xi_{viscous}$ and, consequently, $\xi_{eq,total}$, to evolve consistently with damage accumulation and structural softening. By embedding this cycle-dependent stiffness degradation into an energy-based damping evaluation, the proposed procedure overcomes a central limitation of traditional EVDR methods and provides a more physically transparent description of damping in degrading RC frames. The degraded stiffness over cycles is calculated as:

$$K_i = K_0\left(\Delta_y/\Delta_m\right)^{\alpha} \tag{5}$$

where K_i is the unloading stiffness in cycle i, K_0 is the initial elastic stiffness, Δ_y is the yield displacement, Δ_m is the maximum displacement experienced per cycle, and α is the unloading stiffness coefficient, taken as 0.5 in this study.

The yield displacement was determined from the nonlinear dynamic analysis by monitoring the evolution of longitudinal reinforcement stress throughout the time-history response. The yield criterion was defined as the instant when the average longitudinal steel stress in critical regions first reached the specified yield stress (f_y), following the approach adopted by Peng and Guner [32] for direct displacement-based seismic assessment of concrete frames.

4. Material Characteristics and Finite Element Discretization

4.1. Materials

4.1.1 Concrete Stress-Strain Relation

The nonlinear behavior of concrete is modeled using the Concrete Damage Plasticity Model (CDPM), incorporating a constitutive law for compression based on Hafezolghorani et al. [33].

$$\sigma_c = \sigma_{cu}\left[2\left(\frac{\varepsilon_c}{\varepsilon_c'}\right) - \left(\frac{\varepsilon_c}{\varepsilon_c'}\right)^2\right] \tag{6}$$

where σ_c and ε_c represent the compressive stress and strain, respectively, and σ_{cu} and ε_c' denote the ultimate compressive strength and strain of unconfined concrete.

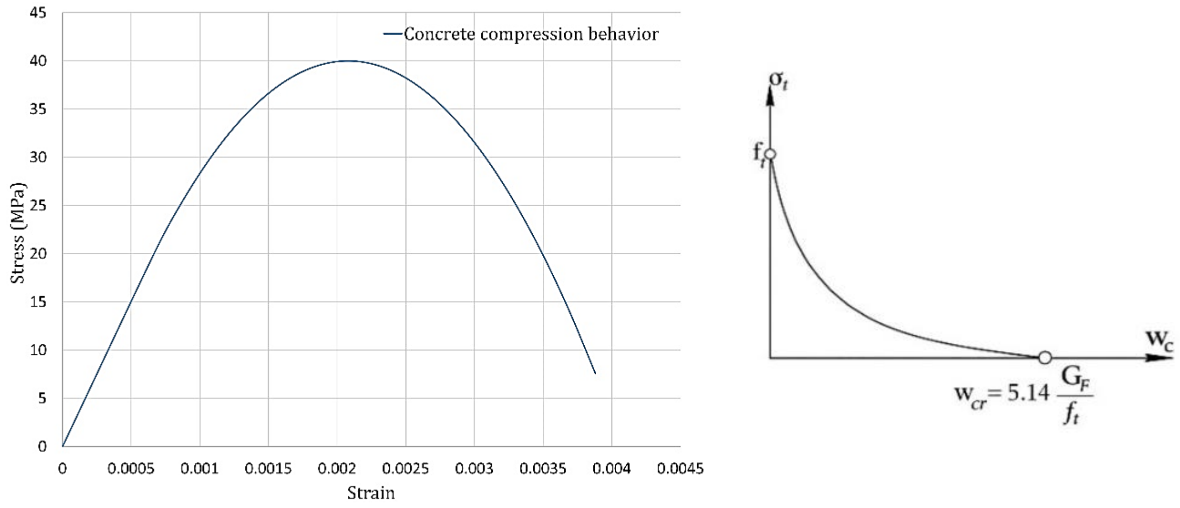

(a) (b)

Fig. 3. (a) Concrete uniaxial compressive stress-strain diagram; (b) stress–crack opening diagram for uniaxial concrete in tension [34, 35]

The tensile behavior of concrete is modeled using an exponential softening law to capture the progressive degradation of tensile stress as a function of crack opening displacement. This formulation is based on the crack-opening model proposed by Cornelissen et al. [34], which defines the relationship between the normal tensile stress σ_t and the crack opening displacement, w_t, as follows:

$$\frac{\sigma_t}{f_{ct}} = \left[1 + \left(c_1\frac{w_t}{w_{cr}}\right)^3\right]e^{\left(-c_2\frac{w_t}{w_{cr}}\right)} - \frac{w_t}{w_{cr}}(1 + c_1^3)e^{(-c_2)} \tag{7}$$

In this expression, f_{ct} denotes the peak tensile strength, and w_{cr} is the critical crack-opening displacement corresponding to complete tensile stress release. The dimensionless softening parameters are taken as $c_1 = 3.00$ and $c_2 = 6.93$, as recommended in the original model [34].

The associated fracture energy G_f, representing the energy dissipated per unit of crack surface during complete tensile failure, is evaluated in accordance with the CEB-FIP Model Code 1990 [35]:

$$G_f = G_{f0}\left(\frac{f_{cm}}{f_{cm0}}\right)^{0.7} \tag{8}$$

where $f_{cm} = f_{ck} + 8$ MPa denotes the mean compressive strength of concrete, and $f_{cm0} = 10$ MPa is the reference strength.

Moreover, the CDP model enables progressive damage analysis of concrete by introducing a scalar damage variable, "*d*", ranging from 0 (undamaged) to 1 (fully damaged or fractured). The model distinguishes two damage parameters: d_c for compression-induced damage and d_t for tension-induced damage, each quantifying the reduction in elastic modulus associated with crushing and cracking, respectively.

Under cyclic loading, concrete exhibits complex degradation behavior characterized by repeated opening and closing of microcracks. The CDPM in Abaqus/CAE captures the asymmetric stiffness recovery of concrete under reversible loading by using independent recovery parameters, w_t for tension and w_c for compression, to control the degree of stiffness regained upon load reversal. The effective elastic modulus is governed by $E = (1 - d_t) E_0$ in the compression branch following tensile damage and by $E = (1 - d_t) (1 - d_c) E_0$ in the tension branch after compressive crushing. The default Abaqus/CAE stiffness recovery parameters ($w_t = 0, w_c = 1$) specify complete compressive stiffness restoration upon crack closure while preventing tensile stiffness recovery following compressive crushing. Figure 4 illustrates the stress-strain response under a complete tension-compression-tension loading cycle.

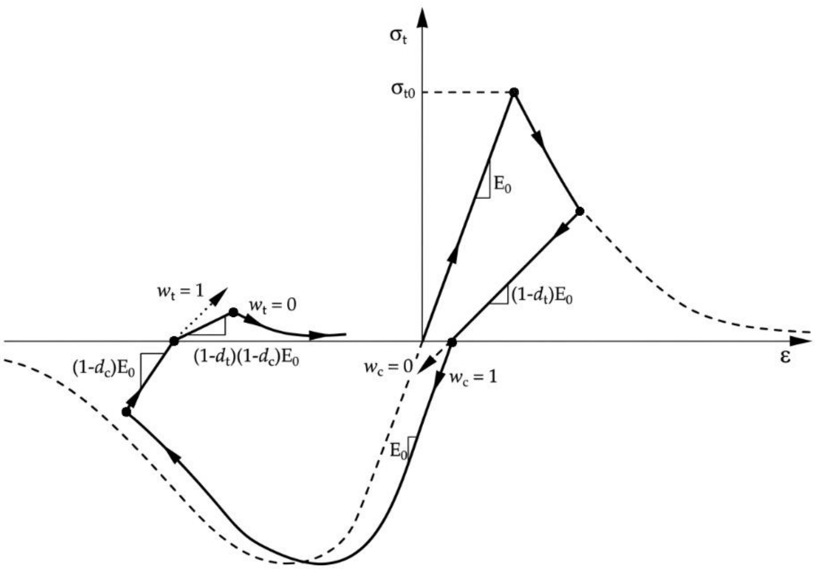

Fig. 4. Uniaxial cyclic behavior [22]

Sinha et al. [36] showed that concrete cylinders under cyclic loading exhibit significant stiffness degradation at a critical compression damage value of $d_c = 0.30$. This threshold aligns with findings from multiple CDP model studies that associate this value with severe crushing and is therefore adopted as the concrete crushing criterion in this study [37].

4.1.2 Properties of Steel Reinforcement and Steel-Concrete Interaction

HRB400 steel reinforcement (nominal yield strength f_y = 400 MPa) was used for all structural members. Steel behavior was modeled using a Chaboche-type combined isotropic–kinematic hardening plasticity law based on the von Mises yield criterion. This formulation captures key nonlinear cyclic phenomena, including the Bauschinger effect and cyclic hardening or softening through concurrent translation and expansion of the yield surface. All hardening parameters were adopted from Lu et al. [38]. A perfect bond was assumed at the concrete–steel interface.

4.2. Finite Element Meshing and Discretization Strategy

Concrete was discretized using eight-node linear brick solid elements with reduced integration (C3D8R) to mitigate shear locking and accurately capture flexural deformations in RC joint regions [39]. Steel reinforcement was modeled using two-node truss elements (T3D2), whereas CFRP layers were modeled using four-node reduced-integration shell elements (S4R) with orthotropic material properties defined for each ply.

5. Modal Analysis

A modal analysis using the Lanczos method in Abaqus/CAE [22] was performed to assess the dynamic characteristics of both the primary and the CFRP-retrofitted structures, assuming linear elastic material behavior for all frames. The first four eigenfrequencies were extracted and evaluated, as shown in Table 2. Rayleigh damping coefficients were calculated using the first and third vibrational modes. This mode selection ensured that the cumulative mass participation in the X-direction (Fig. 1), which aligns with the direction of the imposed base excitation, exceeded 95%.

Table 2. Comparison of modal characteristics: Primary vs. CFRP-retrofitted frames

Mode	Primary frame		CFRP retrofitted frame (Configuration A)		CFRP retrofitted frame (Configuration B)	
	Eigen frequencies (Cycle/time)	Mass participating ratio in X direction (%)	Eigen frequencies (Cycle/time)	Mass participating ratio in X direction (%)	Eigen frequencies (Cycle/time)	Mass participating ratio in X direction (%)
1	2.89	82.43	2.91	82.42	2.94	82.54
2	9.62	12.21	9.68	12.21	9.76	12.16
3	17.52	5.36	17.58	5.37	17.68	5.30
4	26.01	0.0	26.04	0	26.10	0

A comparison of the modal characteristics of the primary and CFRP-retrofitted frames showed only minor variations in natural frequencies and modal mass participation ratios across all extracted modes. This suggests that CFRP retrofitting did not significantly alter the global linear elastic stiffness of the frames. Consequently, the differences observed in the subsequent nonlinear IDA can be attributed primarily to changes in post-elastic behavior induced by the retrofit.

Moreover, the near equivalence in natural frequency between the primary and retrofitted frames enables a fair comparison of their energetic behavior under identical sinusoidal base displacements. This similarity ensures that any differences in structural response observed during IDA can be confidently attributed to the CFRP retrofit rather than to resonance effects arising from a mismatch between the imposed excitation frequency and the natural frequency of each frame.

6. Nonlinear Model Validation Procedure

An energy-based validation procedure was developed to assess the accuracy of the nonlinear primary frame model by comparing its response to that of an equivalent linear system. The comparison was based on two critical parameters, the effective stiffness K_{eff} and the EVDR, following the methodology outlined in [40].

The nonlinear primary frame was subjected to harmonic base excitation at its fundamental frequency, defined as $u(t) = A\ sin(\omega t)$ with $\omega = \omega_n$. The displacement amplitude, A = 6 mm, was calibrated so that the model reached the specified threshold after 14 consecutive loading cycles. A 5% damping ratio was assigned using Rayleigh damping coefficients. Figure 5 shows the time history of the primary frame's top displacement response.

Since the validation procedure aims to verify the nonlinear frame behavior through comparison with its linear substitute model, the accuracy of the linear model must first be established. To this end, the linear substitute model was subjected to the same base displacement excitation as the nonlinear frame, and the EVDR was evaluated using the strain energy method once a stable cyclic response had been achieved. The analysis yielded an EVDR of approximately 4.8%, closely matching the prescribed 5% damping ratio. This confirms that the linear model accurately captures the prescribed damping characteristics and can therefore be considered fully validated for use as a reliable reference in the subsequent nonlinear model evaluation.

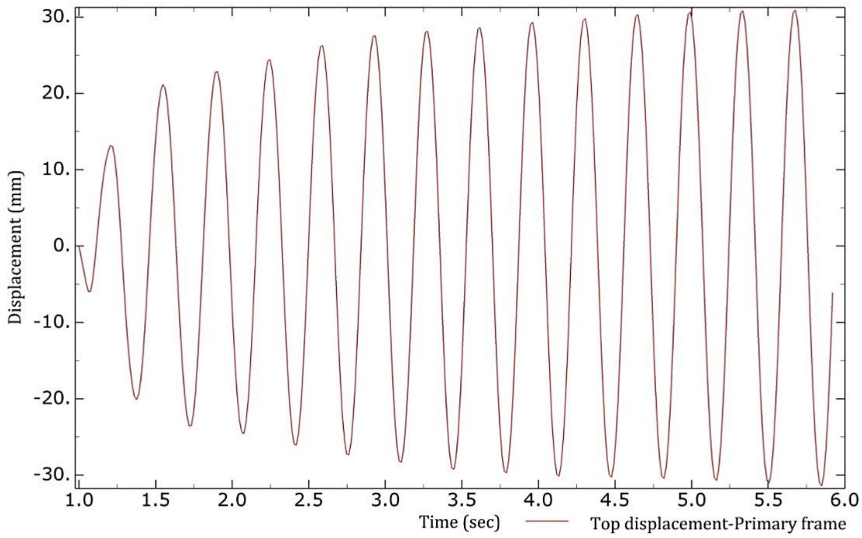

Fig. 5. Top displacement response of the primary frame subjected to sinusoidal base displacement at its resonance frequency

The validation procedure for the nonlinear frame consisted of four sequential steps:

- Ductility assessment: The displacement ductility ratio $\mu = \Delta_m/\Delta_y$ was evaluated based on the final three cycles of the nonlinear response, during which the frame exhibited stable inelastic behavior with peak displacement amplitudes approximately equal to Δ_m.
- Damping assignment: The average EVDR computed from the last three cycles of the nonlinear response was assigned to the linear substitute model, which was then subjected to the same base displacement input as the nonlinear frame.
- Stiffness reduction: The linear substitute model was initially assigned the elastic stiffness K_0 and subjected to the same base excitation as the nonlinear frame. To account for inelastic stiffness degradation, the elastic stiffness of the linear model was reduced using the Takeda degradation ratio, computed from the mean unloading stiffness degradation observed over the last three stabilized cycles of the nonlinear response. This stiffness adjustment was applied together with the EVDR specified in step 2, ensuring a consistent representation of both stiffness and energy dissipation characteristics in the linear model. Once the linear model reached a steady-state response, the peak roof displacement was extracted and systematically compared with the mean value of Δ_m obtained from the last three cycles of the nonlinear analysis. Close agreement between the linear and nonlinear responses, specifically matching peak displacement within an acceptable tolerance, confirmed that the equivalent linear model adequately captured the essential inelastic behavior.
- Energetic verification: The energy dissipated per cycle during the steady-state response (corresponding to the attainment of Δ_m) was computed for the linear elastic model and compared with the average per-cycle energy dissipation observed over the final three cycles of the nonlinear analysis. The corresponding energy dissipation values at the associated peak roof displacement are summarized in Table 3.

Table 3. Comparison of energy dissipation between the nonlinear primary frame model and the linear substitute model

Average $\xi_{eq,total}$ over the last three cycles (%)	Maximum top displacement Δ_m reached in the nonlinear model (mm)	Reduced frequency in the equivalent linear substitute model (Hz)	Top displacement in the equivalent linear substitute model (mm)	Average dissipated energy in the nonlinear model over the last three cycles (J)	Dissipated energy in the linear substitute model per cycle at steady-state response (J)
9.72	31.4	2.63	31	1.3×10^3	1.36×10^3

The results showed that the nonlinear primary frame accurately captured the expected energy dissipation behavior when compared with the validated linear reference model. This consistency indicates that the nonlinear model provides a reliable representation of the inelastic response under cyclic loading, confirming its adequacy for subsequent dynamic analysis.

7. Results and Discussion

7.1. Energy-Based Performance Evaluation of Configuration A (Flange-Bonded CFRP) Under Resonant Loading

7.1.1 Energy Dissipation Characteristics

A comparative analysis of energy dissipation mechanisms was conducted for the primary frame and its CFRP-retrofitted counterpart employing Configuration A under resonant excitation conditions. The IDA revealed an unexpected outcome: the retrofitted frame reached its ultimate member curvature after only 10 cycles, compared to 14 cycles sustained by the primary frame before failure.

Cycle-by-cycle energy analysis during the common operational period (cycles 1–10) showed that the retrofit significantly altered the system's energy dissipation mechanisms (Fig. 6). The retrofitted frame exhibited higher E_{se} and E_v than the primary frame, with increases of approximately 67% and 48%, respectively, by cycle 10. However, E_p in the retrofitted system increased at a slower rate, resulting in a reduction of up to 20% relative to the primary frame by the tenth cycle, indicative of ongoing stiffness degradation. According to Akbas et al. [41], both E_k and E_{se} constitute relatively small portions of E_{input} at any given time during the vibrational response. Consequently, E_v and E_{hyst} emerge as the dominant contributors to input energy dissipation.

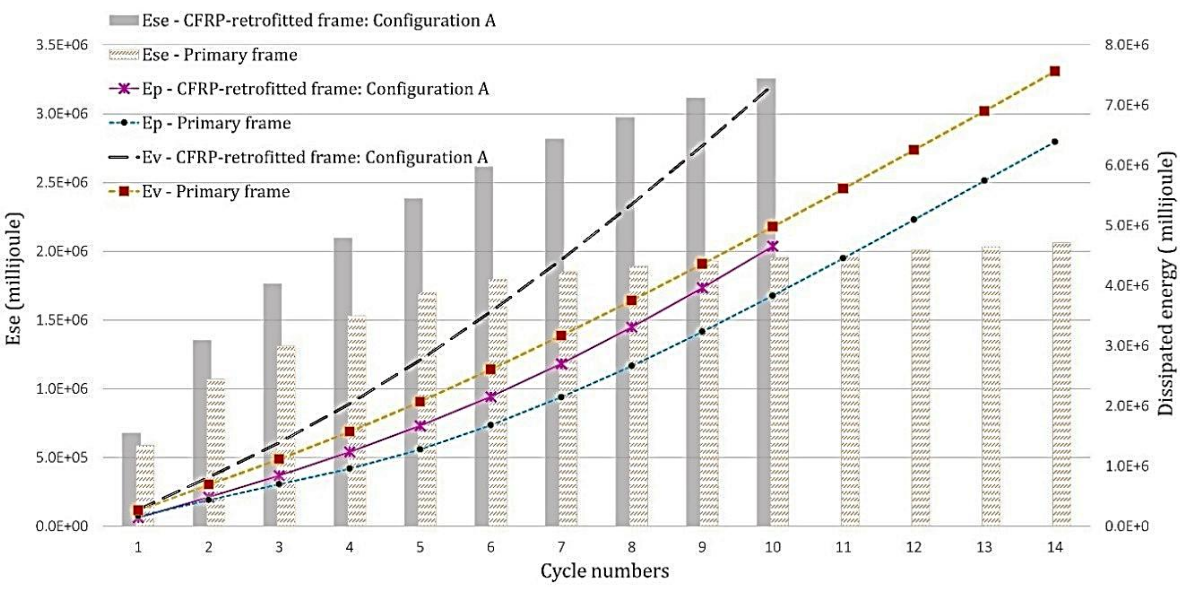

Fig. 6. Maximum elastic strain energy per cycle and cumulative viscous and plastic energy dissipation at resonance: primary vs. Configuration A CFRP-retrofitted frame

Over the full loading history, both E_v and E_p were consistently higher in the CFRP-retrofitted frame than in the primary frame, indicating that the retrofit enabled the structure to attract more E_{input} across cycles. The associated increase in input energy demand was accommodated primarily through greater viscous energy dissipation rather than additional inelastic hysteretic dissipation, as evidenced by the significantly higher accumulation rate of E_v in the retrofitted configuration. These findings indicate that CFRP retrofitting alters the energy dissipation mechanism, with a larger portion of the input energy temporarily stored as recoverable elastic strain energy and subsequently dissipated through viscous damping, thereby reducing reliance on inelastic hysteretic mechanisms.

7.1.2 Equivalent Viscous Damping Ratio Evolution

Analysis of the EVDR components revealed distinct damping characteristics between the CFRP-retrofitted and the primary frames (Fig. 7(a)). Both systems exhibited a transient decrease in $\xi_{viscous}$ and ξ_{hyst} during the initial loading cycles, reflecting structural adaptation to cyclic excitation. Following this phase, $\xi_{viscous}$ converged to approximately 5% in both frames, consistent with the assigned inherent damping ratio, whereas ξ_{hyst} evolved differently.

The primary frame showed progressive growth in ξ_{hyst} from 2.7% at cycle 4 to 5% at cycle 11, maintaining this plateau through cycle 14. In contrast, the CFRP-retrofitted frame achieved early stabilization of ξ_{hyst} within the narrow range of 2.8–3.2% after only four consecutive cycles, representing an approximately 40% reduction relative to the peak ξ_{hyst} observed in the primary frame. As a result, the CFRP retrofit reduced the overall EVDR, driven primarily by lowering ξ_{hyst}. This reduction stems from the higher E_{se} of the retrofitted frame, which results in a smaller fraction of E_{input} being dissipated through hysteretic mechanisms and a larger fraction being stored and released elastically, consistent with the energy-based observations previously established in Fig. 6.

Time-history analysis of roof displacements revealed that the retrofitted frame exhibited greater displacement responses than the primary frame (Fig. 7(b)). Given the lower EVDR induced by the retrofit, this behavior is consistent with the dynamic response of systems operating under resonance conditions, where damping plays a critical role in controlling displacement amplitudes [42]. In fact, a lower EVDR indicates the structure is more elastic (storing more E_{se}) but less damped, and therefore dissipates vibrational energy less effectively per cycle, resulting in larger oscillatory displacements.

A cycle-by-cycle evaluation of the maximum base shear values (V_{max}) showed that the retrofitted frame consistently exhibited higher V_{max} in each cycle than the primary frame (Fig. 7(a)). The concurrent increase in roof displacement and V_{max} resulted in substantially greater E_{se} per cycle in the retrofitted system, thereby increasing member force demands, particularly in the CFRP-retrofitted members. This behavior highlights the need for appropriate CFRP detailing and local strengthening measures to accommodate the additional force demands that develop under resonant excitation. Nonetheless, the observed premature failure of the retrofitted frame relative to its primary counterpart suggests potential limitations of the adopted retrofit configuration.

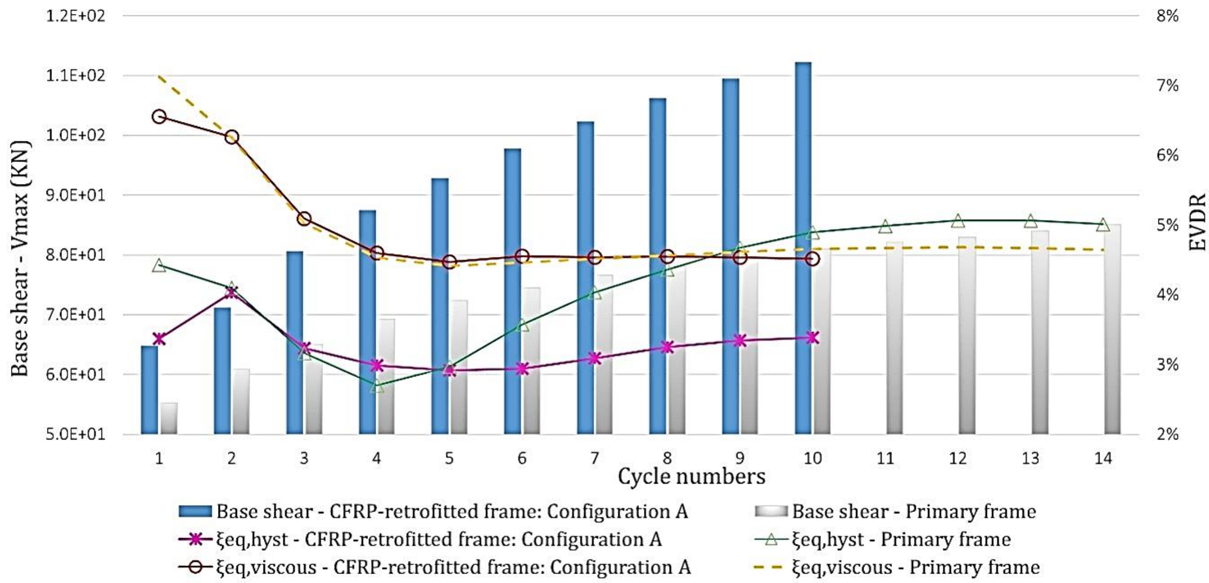

(a)

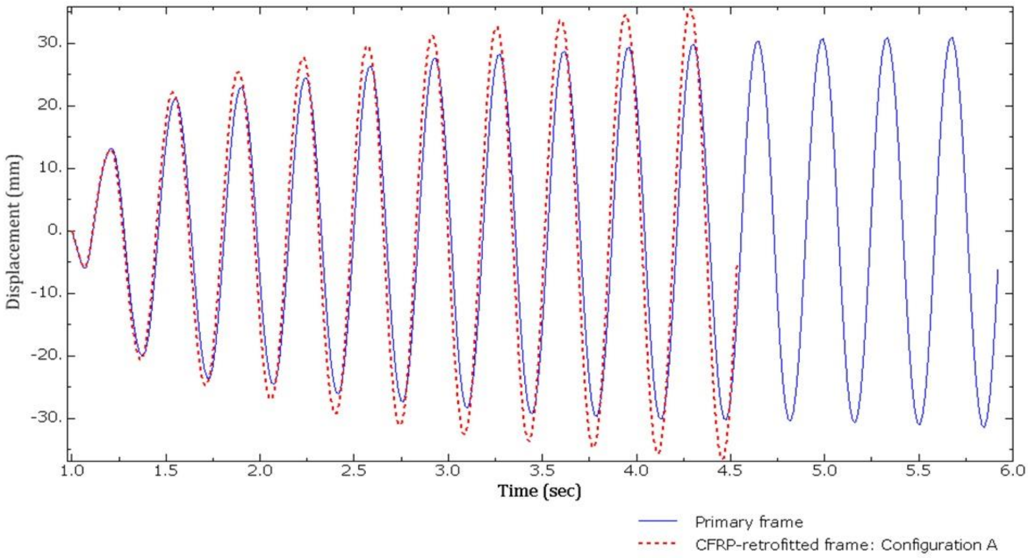

(b)

Fig. 7. Primary vs. Configuration A CFRP-retrofitted frame under resonance-frequency excitation: (a) evolution of EVDR and V_{max} at resonance; (b) comparative top displacement responses

Finite element analyses showed that elevated member forces triggered crack-induced delamination at the beam–column interface, substantially compromising stress transfer between the flange-bonded CFRP laminates and the reinforced concrete substrate. In combination with amplified dynamic forces, this mechanism precipitated premature plastic hinge formation in beam segments adjacent to the joint (Fig. 8). Consequently, the retrofitted frame reached its ultimate curvature limit earlier than the primary frame, resulting in localized member failure at the beam–column interface. This counterintuitive result indicates that, under resonant excitation, CFRP retrofitting may reduce structural endurance when amplified dynamic forces cause premature interface delamination and localized member failure before the retrofitted system's intended capacity is fully mobilized.

To address these limitations, engineers should consider alternative strengthening strategies that employ selective retrofit configurations. These configurations should be designed to limit excessive deformation at critical beam–column interfaces by promoting plastic hinge redistribution and shifting inelastic strains away from vulnerable joint regions. Configuration B, analyzed later in this study, exemplifies this approach by demonstrating how targeted retrofitting can redistribute plastic deformation away from vulnerable beam-column interfaces while controlling the magnitude of the force amplification that led to premature failure in Configuration A.

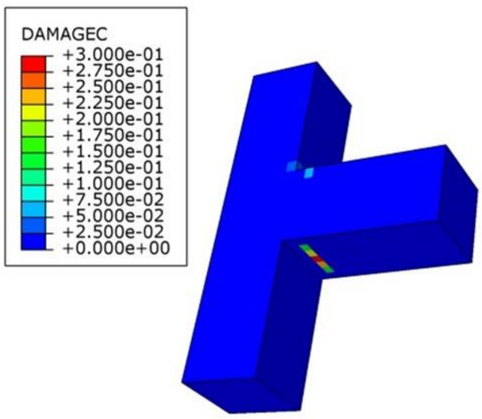

Fig. 8. Ultimate curvature at the beam-column interface following Configuration A after local CFRP delamination

7.2. Comparative Analysis of CFRP Flange-Web Bonded Configuration: Enhanced Performance Through Plastic Hinge Relocation

7.2.1 Energy Dissipation Characteristics

The energy dissipation characteristics of Configuration B, featuring reduced CFRP length ($L_f = 0.67h_b$) and combined flange-web bonding (Fig. 1(b)), were evaluated under identical sinusoidal base displacement $u(t) = 6\ sin(\omega t)$ to enable direct comparison with Configuration A. In all remaining energy-related plots in this study, the response histories were truncated after 20 loading cycles, as this range was sufficient to capture the essential energy dissipation trends, rendering additional cycles less informative for comparative analysis.

Comparative energy analysis over the shared cycle range (cycles 1–10; Fig. 9(a)) showed that Configuration A mobilized higher E_{se} and greater cumulative E_v than Configuration B, with maximum increases of approximately 33% and 22%, respectively, by cycle 10. During this interval, both configurations exhibited comparable E_p levels. Beyond cycle 10, E_{se}, E_v, and E_p components in Configuration B continued to increase steadily throughout the remaining cycles.

The key performance distinction between the two CFRP-retrofitted configurations lies in their cyclic durability. Configuration B demonstrated significantly greater endurance, withstanding 22 consecutive loading cycles before reaching the ultimate curvature limit, compared with only 10 cycles for Configuration A. This enhanced cyclic durability is attributed to the successful relocation of the plastic hinge achieved through the modified CFRP layout. By strategically limiting the flange-bonded length and incorporating web-bonded reinforcement, Configuration B redistributed plastic strain accumulation away from the vulnerable beam–column interface toward the CFRP termination region. Longitudinal beam reinforcement strain measurements confirmed this redistribution: steel rebars at the CFRP termination point exhibited significant plastic strains, whereas those within the CFRP-covered zone showed minimal inelastic deformation (Fig. 10).

Moreover, energy-based response evaluation of the primary frame and the CFRP-retrofitted Configuration B (Fig. 9(b)) revealed dynamic trends consistent with those observed in Configuration A, with progressive increases in both recoverable and dissipative energy components across loading cycles. By cycle 14, Configuration B exhibited approximately 30% higher maximum per-cycle E_{se}, 23% higher E_v, and 14% higher E_p than the primary frame. Although these increases were less pronounced than those observed in Configuration A, they nonetheless represent substantial improvements in both E_{se} and E_v relative to the primary frame, with only a moderate increase in E_p across the 14-cycle range.

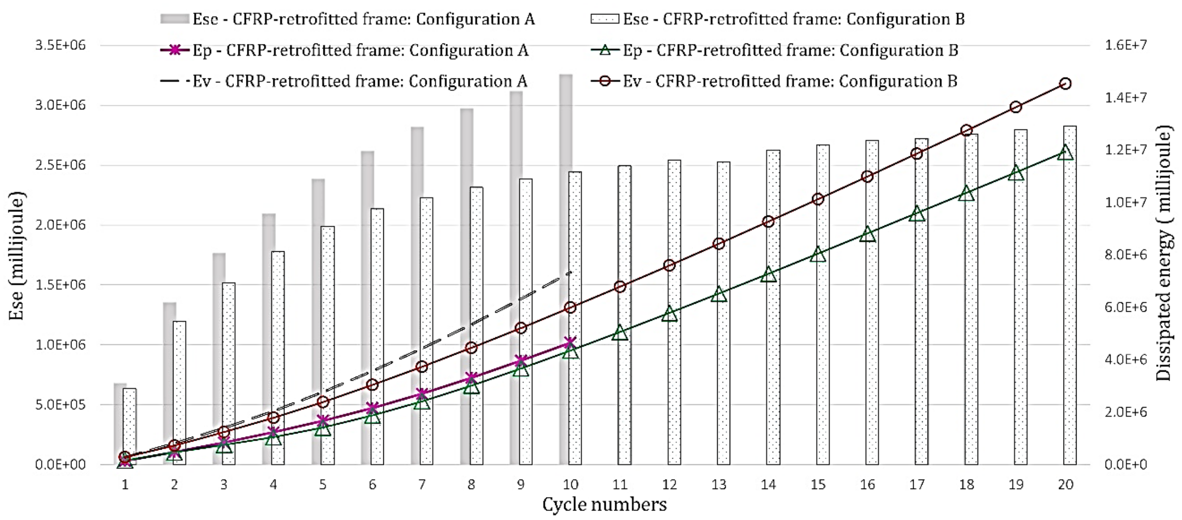

(a)

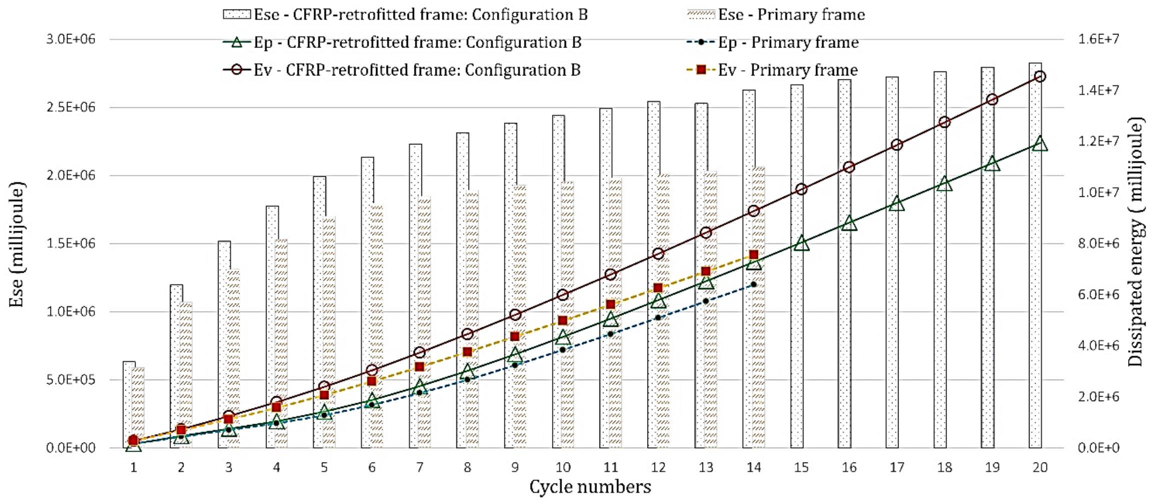

(b)

Fig. 9. Maximum elastic strain energy per cycle and cumulative viscous and plastic energy dissipation at resonance: (a) Configuration A vs. Configuration B CFRP-retrofitted frames; (b) primary vs. Configuration B CFRP-retrofitted frame

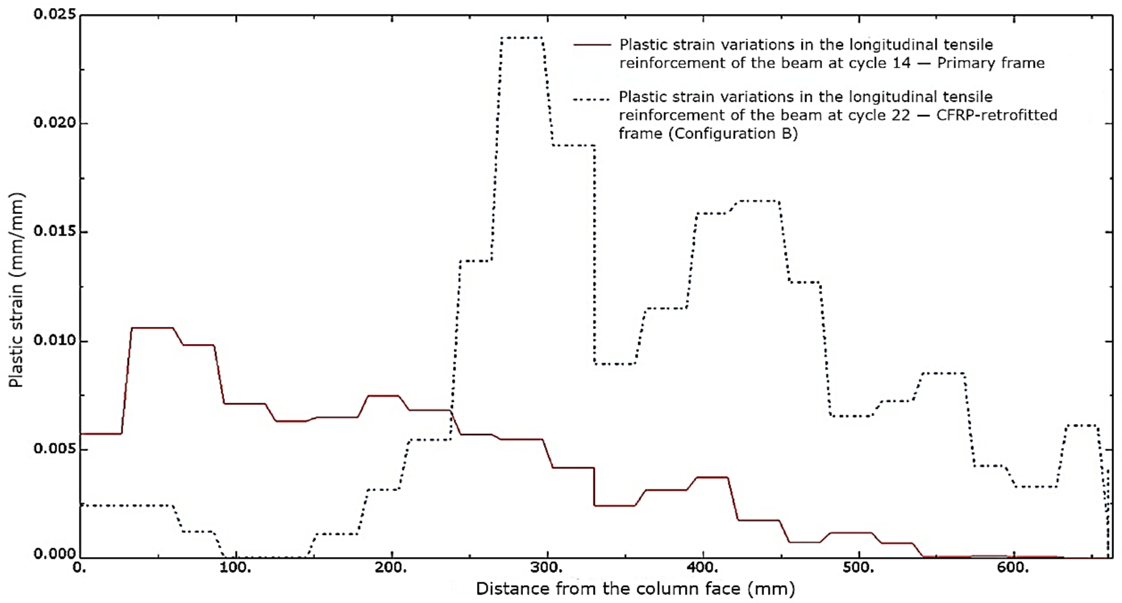

Fig. 10. Strain variation in longitudinal beam reinforcement: primary vs. Configuration B CFRP-retrofitted frame

7.2.2 Equivalent Viscous Damping Ratio Evolution

Comparison between Configurations A and B reveals distinct EVDR characteristics (Fig. 11). In both cases, $\xi_{viscous}$ converged to the assigned 5% inherent damping ratio following the initial transient cycles. However, the evolution of the hysteretic component differed significantly. Configuration B exhibited a gradual increase in ξ_{hyst}, rising from 2.7% at cycle 4 to approximately 4.6% by cycle 10 before stabilizing in the remaining cycles. In contrast, Configuration A consistently showed lower ξ_{hyst} values, plateauing between cycles 8 and 10 at 2.8% to 3.2%, as previously noted. This indicates a markedly reduced reliance on hysteretic energy dissipation in Configuration A relative to Configuration B. Moreover, the cycle-by-cycle increase in V_{max} was less pronounced in Configuration B than in Configuration A, indicating lower force demands on the RC members. This reduction in force demand, coupled with the strategic relocation of plastic hinges away from critical joint regions, mitigated early member failure and enhanced the frame's capacity to sustain cyclic deformation. In summary, under resonant sinusoidal excitation, CFRP retrofitting significantly altered the frame's energy dissipation behavior. Both configurations increased E_{se} and shifted energy dissipation toward viscous mechanisms. However, these improvements were accompanied by a reduction in overall EVDR and increased internal force and base shear demands, with the severity of these effects strongly dependent on the adopted retrofit configuration.

Configuration A, which used continuous flange bonding with an extended development length ($L_f = 2h_b$), achieved the highest E_{se} but also caused delamination at the CFRP–concrete interface, leading to premature member failure relative to the primary frame. In contrast, Configuration B mitigated these adverse effects by limiting the flange-bonded length and adding web-bonded reinforcement, thereby promoting plastic hinge relocation and redistributing inelastic demands to less critical beam regions. Although it generated lower E_{se} than Configuration A, Configuration B substantially enhanced the frame's cyclic durability by delaying member failure. These findings highlight the importance of balancing increased elastic energy with optimized energy dissipation, manageable force demands, and controlled damage mechanisms to enhance overall seismic resilience.

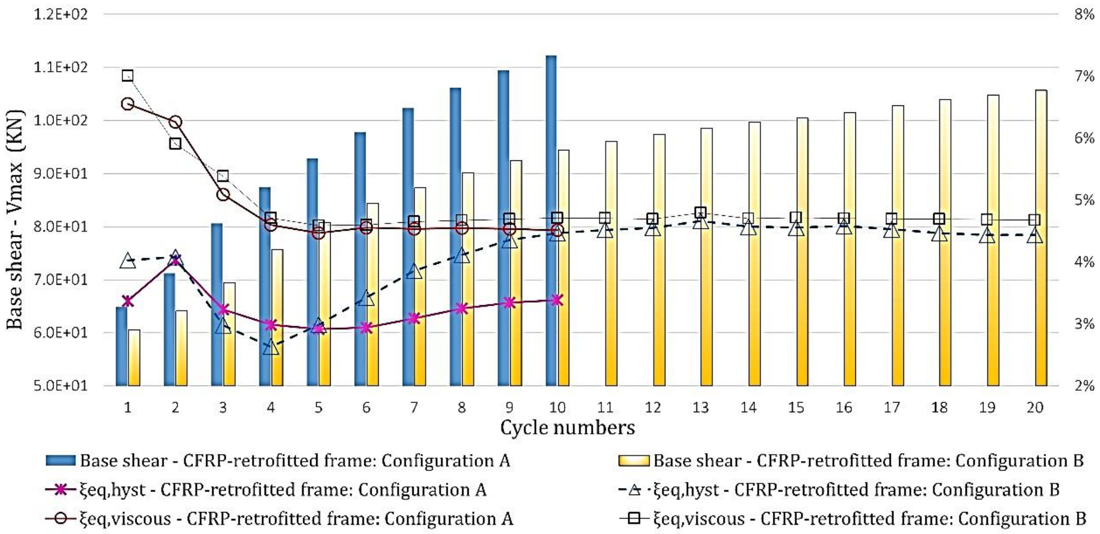

Fig. 11. Cycle-by-cycle evolution of EVDR and V_{max} in CFRP-retrofitted frames under resonance-frequency excitation: Configuration A vs. Configuration B

7.3. Assessment of EVDR Consistency Under Off-Resonance Excitation

To assess whether the EVDR trends observed at resonance also held under off-resonance conditions, a complementary set of analyses was performed. Parametric off-resonance simulations were conducted at frequency ratios of $0.75\omega_n$ (below resonance, B-RES) and $1.25\omega_n$ (above resonance, A-RES). A performance-based calibration procedure, consistent with that used for the resonance case, was implemented to ensure comparable inelastic demand in the primary frame across all excitation frequencies. For each frequency ratio, the sinusoidal base displacement amplitude was iteratively adjusted until the primary frame reached its ultimate curvature limit state after 14 loading cycles. The same calibrated displacement history was then applied to the CFRP-retrofitted configuration, enabling a direct comparison of energy partitioning under identical base excitations. The resulting calibrated base displacement amplitudes were $A_{B\text{-}RES}$ = 11.8 mm and $A_{A\text{-}RES}$ = 12.5 mm for the below-resonance and above-resonance conditions, respectively.

This methodology ensures that observed variations in EVDR are primarily attributable to frequency effects rather than to differences in structural deformation demand. Four simulation cases were analyzed: B-RES-primary, B-RES-CFRP, A-RES-primary, and A-RES-CFRP. Following the comparative assessment of energy dissipation behavior previously performed at resonance, Configuration B was selected as the CFRP retrofit configuration for off-resonance analyses. Its superior cyclic durability makes it a more representative and practical solution for seismic retrofit applications, justifying its use for subsequent off-resonance investigations. Figure 12 shows the evolution of the principal energy components (E_{se}, E_v, and E_p), along with the corresponding EVDR values, for both the below-resonance and above-resonance cases.

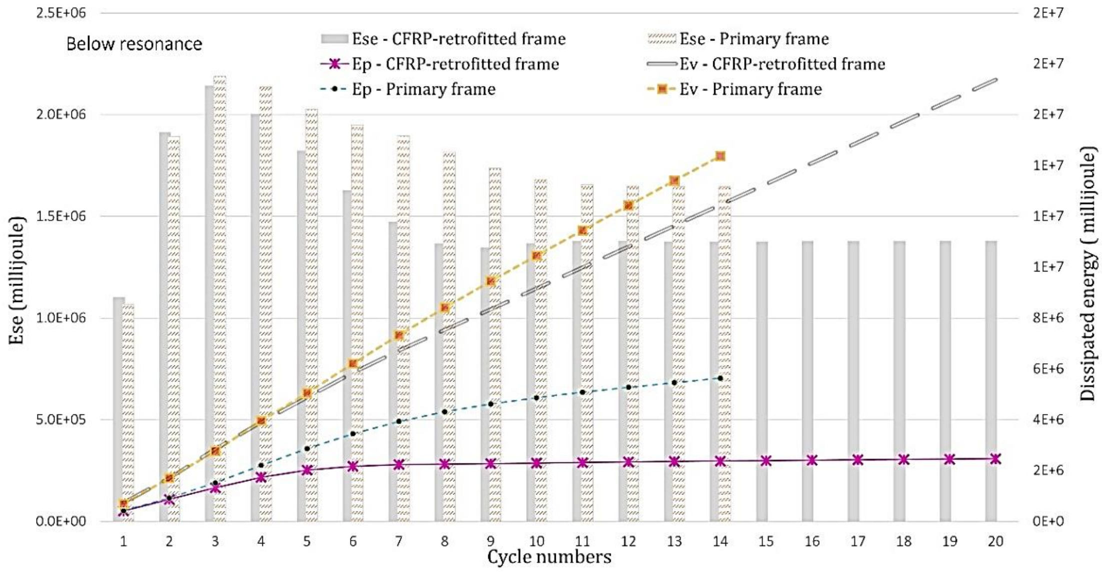
Below resonance
Ese - CFRP-retrofitted frame
Ese - Primary frame
Ep - CFRP-retrofitted frame
Ev - CFRP-retrofitted frame
Ep - Primary frame
Ev - Primary frame
Ese (millijoule)
Dissipated energy (millijoule)
Cycle numbers

(a)

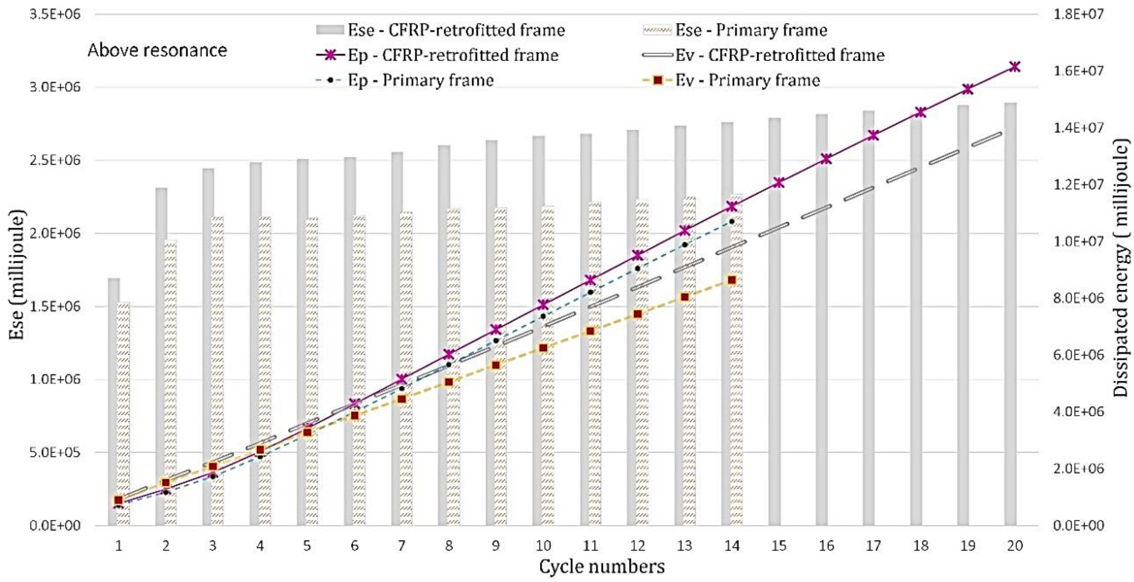
Above resonance
Ese - CFRP-retrofitted frame
Ese - Primary frame
Ep - CFRP-retrofitted frame
Ev - CFRP-retrofitted frame
Ep - Primary frame
Ev - Primary frame
Ese (millijoule)
Dissipated energy (millijoule)
Cycle numbers

(b)

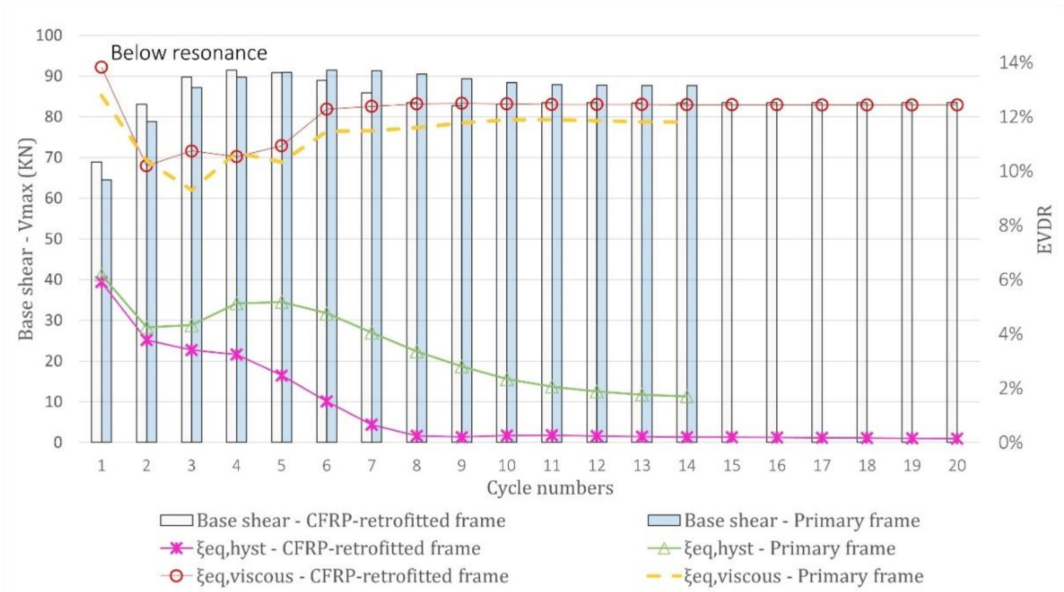
Below resonance
Base shear - Vmax (KN)
EVDR
Cycle numbers
Base shear - CFRP-retrofitted frame
Base shear - Primary frame
ξeq,hyst - CFRP-retrofitted frame
ξeq,hyst - Primary frame
ξeq,viscous - CFRP-retrofitted frame
ξeq,viscous - Primary frame

(c)

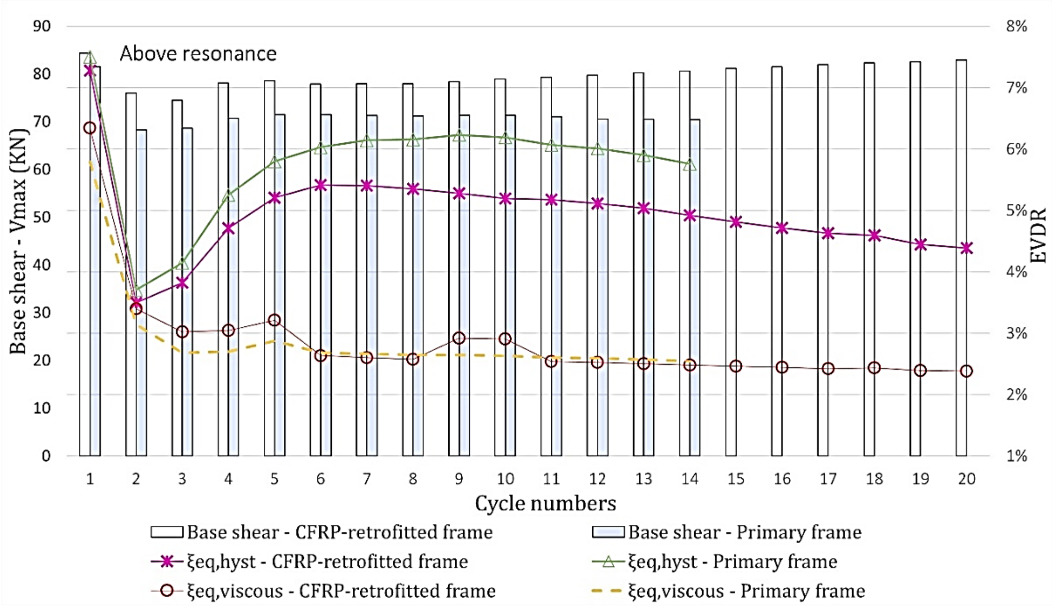

(d)

Fig. 12. Off-resonance response for the primary and CFRP-retrofitted frames: (a, b) maximum elastic strain energy per cycle and cumulative viscous and plastic dissipation; (c, d) cycle-by-cycle evolution of EVDR and V_{max}

7.3.1 Energy Dissipation Characteristics

Under below-resonance excitation, fundamental differences in energy dissipation mechanisms emerged between the primary and CFRP-retrofitted frames. The retrofitted frame exhibited superior cyclic durability, withstanding more than 20 loading cycles without reaching its ultimate curvature limit (Fig. 12(a)). Cycle-by-cycle comparison revealed that the retrofitted frame exhibited a rapid increase in E_p, followed by a clear plateau at approximately 2.4×10^6 mJ from around cycle 6 onward. This plateau indicates the cessation of plastic dissipation, consistent with elastic shakedown behavior, where further stiffness degradation is not expected. In contrast, the primary frame showed continuous growth of E_p, reaching approximately 5.6×10^6 mJ by cycle 14, indicative of progressive structural deterioration. Following the onset of elastic shakedown, the retrofitted frame transitioned to a purely viscous-dominated energy dissipation regime, reflecting the retrofit's ability to suppress plastic mechanisms and promote a predominantly elastic, non-damaging response under these loading conditions.

Throughout the loading protocol, the CFRP-retrofitted frame consistently exhibited lower values of both E_v and E_{se} than the primary frame. By cycle 14, the retrofitted system had accumulated approximately 1.24×10^7 mJ of E_v, about 16% less than the primary frame, and continued to increase linearly thereafter. From around cycle 8 onward, both systems reached a stable peak E_{se} for the remaining cycles, with the retrofitted frame sustaining a value near 1.38×10^6 mJ, approximately 20% lower than the peak value observed in the primary frame. Neglecting the minor contributions of both E_{se} and E_k relative to E_{input} [41], the CFRP-retrofitted frame dissipated less total energy than the primary frame over the shared cycle interval, indicating that less E_{input} was imparted to the system.

Comparative analysis of the response histories indicates that the retrofitted frame exhibited markedly lower peak roof displacements than the primary frame (Fig. 13), while maintaining comparable V_{max} values (Fig. 12(c)). This combination of reduced displacement demand and similar base shear response reflects an enhancement in the global secant stiffness, defined here as the ratio of V_{max} to the corresponding roof displacement, resulting from the CFRP retrofit. The response behavior observed in the retrofitted frame is consistent with a stiffness-controlled regime, which typically occurs when the excitation frequency lies well below the structure's fundamental frequency. In such regimes, displacement amplitudes are primarily governed by the system's restoring stiffness rather than inertial effects [42]. The increased secant stiffness introduced by the retrofit significantly constrained lateral displacements, thereby limiting both the onset and progression of plastic deformation. As a result, the structure rapidly transitioned into an elastic shakedown state, characterized by stable, recoverable elastic behavior under repeated loading. This elastic stabilization effectively curtailed further E_{input} from the ground motion, leading to a corresponding reduction in both E_v and E_{se} components throughout the response duration.

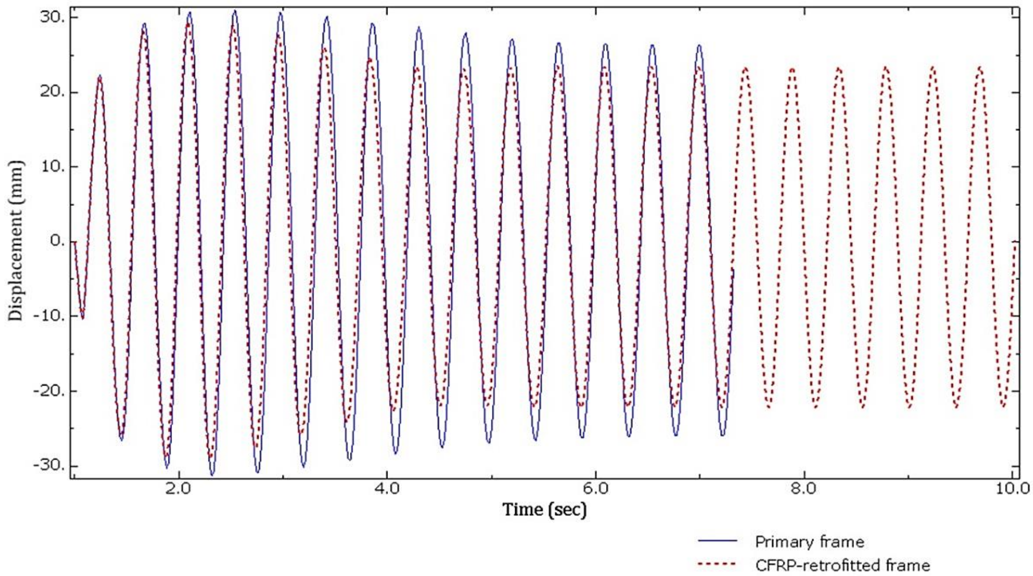

Fig. 13. Top displacement responses of the primary and CFRP-retrofitted frames under below-resonance sinusoidal base excitation

7.3.2 EVDR Response Below Resonance

In the CFRP-retrofitted frame, ξ_{hyst} exhibited pronounced decay after the initial transient cycles. It dropped sharply after the fifth cycle and continued to decrease until it effectively vanished, indicating the cessation of plastic dissipation (Fig. 12(c)). In the primary frame, ξ_{hyst} also began to decrease from approximately the fifth cycle onward; however, its rate of reduction per cycle was lower than in the retrofitted frame and eventually stabilized at a plateau of about 2% before reaching the deformation limit state.

In both frames, $\xi_{viscous}$ converged to relatively high, nearly constant values (approximately 12%), indicating that energy dissipation is predominantly governed by velocity-dependent mechanisms. These results show that, under the stiffness-controlled excitation levels considered, CFRP retrofitting can induce a pronounced shift toward elastic-dominated behavior. The retrofit effectively suppresses inelastic deformation, causing the system to dissipate most of its input energy through viscous mechanisms, whereas the primary frame retains a non-negligible hysteretic contribution.

7.3.3 Energy Partition Trends Above Resonance

At $1.25\omega_n$, the CFRP-retrofitted frame sustained loading up to cycle 28 before reaching its ultimate curvature limit state. Figure 12b shows that E_p remained the dominant energy dissipation mechanism in both frames over the shared 14-cycle interval, in contrast to the behavior observed in the below-resonance regime. However, the retrofitted frame exhibited a slightly higher rate of E_p accumulation, resulting in an overall increase of approximately 5% by cycle 14 relative to the primary frame.

From cycle 8 onward, the retrofitted frame exhibited a steeper rate of increase in E_v, surpassing that of the primary frame by roughly 15% at cycle 14. This progressive cycle-by-cycle increase in total energy dissipation indicates that the retrofit enabled the structure to absorb more E_{input} across cycles [41], consistent with observations under resonance-frequency excitation. Most of this additional energy was dissipated through viscous mechanisms, as also observed in the resonant case.

Regarding E_{se}, the retrofitted system reached a per-cycle peak of approximately 2.76×10^6 mJ by cycle 14. In contrast, the primary frame reached a lower peak of approximately 2.26×10^6 mJ by cycle 4, after which E_{se} plateaued. Beyond the shared cycle range, all energy components of the retrofitted frame continued to increase progressively.

A comparison of the roof displacement histories (Fig. 14) indicates that the two compared frames reached similar peak displacements. In contrast, the cycle-by-cycle base shear records (Fig. 12(d)) show consistently higher base shear forces in the retrofitted frame. This combination of similar displacement levels coupled with higher base shear reflects the enhanced secant stiffness provided by the retrofit. The observed response is indicative of an inertia-controlled regime, which arises when the excitation frequency greatly exceeds the structure's fundamental frequency. In this regime, displacement amplitudes are governed primarily by inertial forces and the frequency content of the ground motion, rather than by the structure's restoring stiffness [42]. Under such conditions, increasing stiffness does not necessarily reduce displacement demands. Instead, the enhanced secant stiffness of the retrofitted frame increased its dynamic coupling with the high-frequency components of the excitation, resulting in amplified acceleration responses and elevated base shear forces. Consequently, greater internal forces and higher E_{se} were generated during each vibration cycle. Additionally, the higher acceleration demands experienced by the retrofitted frame led to an increased velocity response, which, in turn, amplified E_v due to its velocity-dependent nature. However, under these amplified inertial forces, CFRP retrofitting was unable to fully suppress plastic deformation, which continued to develop once inertia-driven response became dominant.

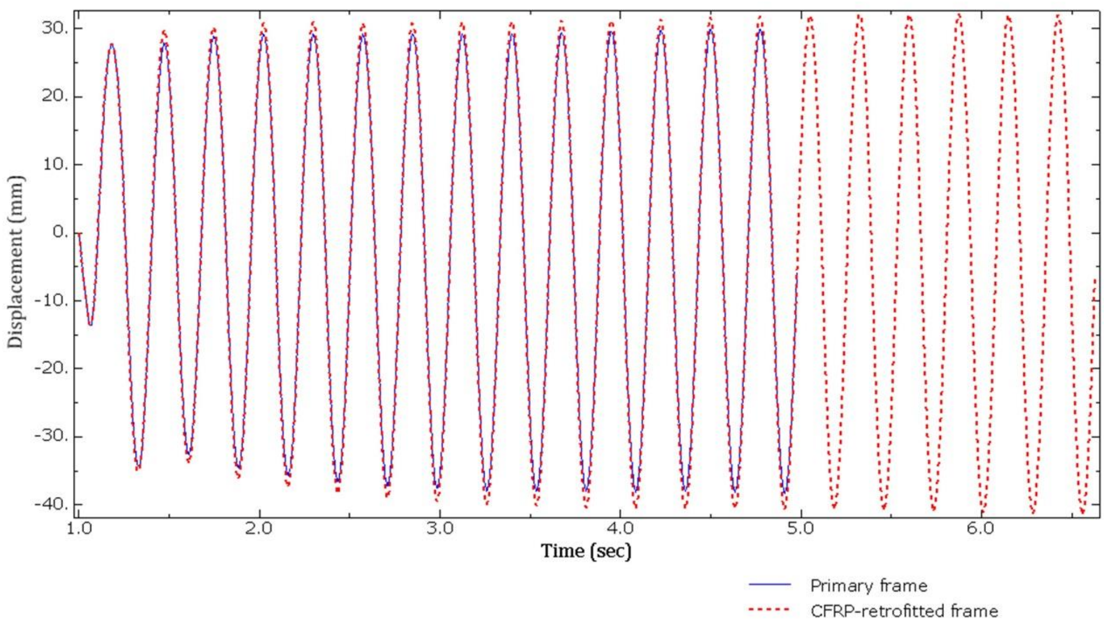

Fig. 14. Top displacement responses of the primary and CFRP-retrofitted frames under above-resonance sinusoidal base excitation

7.3.4 EVDR Response Above Resonance

Excluding the initial transient cycles, ξ_{hyst} in the CFRP-retrofitted frame increased rapidly between cycles 2 and 6, peaking at approximately 4.5% around cycles 6 to 8, before gradually declining in the subsequent cycles (Fig. 12(d)). In contrast, the primary frame exhibited a steeper initial rise in ξ_{hyst}, followed by a relatively stable plateau between 6% and 6.5% up to cycle 14. This consistently lower ξ_{hyst} reflects the enhanced recoverable elastic storage capacity provided by the CFRP retrofit. As a result, a greater proportion of E_{input} is accommodated through recoverable elastic mechanisms rather than irreversible plastic dissipation, as confirmed by the energy response plots (Fig. 12(b)).

Moreover, $\xi_{viscous}$ converged to approximately 2.5% in both frames shortly after the initial cycles, indicating that ξ_{hyst} remained the dominant contributor to the total EVDR.

Although the CFRP retrofit reduced the hysteretic contribution to $\xi_{eq,total}$ compared to the primary frame, this reduction was less significant than in the resonant case and considerably less pronounced than in the below-resonance regime. Consequently, in this regime, the retrofit was comparatively less effective at shifting the primary energy dissipation mechanism away from hysteretic behavior.

8. Conclusions

This study investigated the influence of CFRP retrofitting on the dynamic response of reinforced concrete frames subjected to harmonic base displacement excitation. An energy-based analytical framework was employed to evaluate the influence of various CFRP retrofit configurations on the global structural response, compared with a geometrically and materially identical unretrofitted primary frame under the same loading conditions. The comparative performance of the frames was primarily evaluated through the EVDR, which served as the principal performance indicator. In addition, the study examined the frequency-dependent behavior of CFRP-retrofitted frames, assessing how variations in excitation frequency affect their dynamic response. The key conclusions are:

- Effect of CFRP retrofitting on EVDR: CFRP retrofitting consistently reduced the global EVDR across the range of base excitation frequencies and retrofit configurations examined. However, the magnitude of this reduction was strongly influenced by both the adopted CFRP configuration and the imposed excitation frequency.

- Implications of CFRP configuration on cyclic durability: Results demonstrated the critical role of CFRP retrofit configuration in governing the cyclic durability of reinforced concrete frames. Under resonant excitation, Configuration A, characterized by extended flange-bonded CFRP sheets (e.g., $2h_b$ extensions consistent with ACI 440 guidelines [1]), reduced structural resilience under cyclic loading. This configuration significantly increased elastic energy storage and, in turn, decreased EVDR, thereby amplifying global base shear demands and internal force resultants. The resulting dynamic response promoted premature CFRP delamination and early member failure, effectively negating the intended benefits of the retrofit. In contrast, configurations that intentionally promote controlled plastic hinge relocation away from vulnerable joint zones (achieved by shortening flange-bonded lengths and adding web-bonded reinforcement, as in Configuration B) were shown to mitigate these adverse effects by providing a more favorable balance between moderate gains in elastic energy storage, optimized energy dissipation capacity, and acceptable force and damage demands, thereby enhancing cyclic durability and seismic resilience.

- Frequency-dependent retrofit effectiveness: CFRP retrofitting was found to modify the distribution of energy dissipation across the entire range of excitation frequencies considered. In all cases, a larger portion of the input energy was shifted from inelastic to viscous dissipation mechanisms, reducing the hysteretic contribution to the total EVDR. However, the magnitude of this reduction was highly dependent on the base excitation frequency. CFRP retrofitting was most effective in the stiffness-controlled (below-resonance) range, where it markedly reduced inelastic energy dissipation and promoted an essentially elastic response, thereby suppressing ξ_{hyst}. As the excitation frequency approached and exceeded resonance, this benefit progressively diminished. In the inertia-controlled (above-resonance) regime, ξ_{hyst} regained importance in the retrofitted frame, indicating that a larger share of the E_{input} was still dissipated through inelastic mechanisms despite the retrofit intervention. This frequency-dependent behavior highlights the critical importance of assessing the relationship between a structure's natural frequencies and the anticipated excitation frequency content when designing CFRP-retrofitted systems for seismic applications.

- No impact on linear-elastic properties: CFRP retrofitting preserved the structure's linear-elastic modal characteristics, indicating that it does not significantly alter the global linear-elastic stiffness of the retrofitted frames. Consequently, the performance gains observed in nonlinear dynamic analyses are primarily attributable to modifications in the post-elastic behavior induced by CFRP retrofitting.

Based on the findings of this study, a practical design recommendation is proposed for CFRP-retrofitted RC frames subjected to dynamic loading: to maximize seismic resilience, retrofit strategies should prioritize shorter flange development lengths L_f, which intentionally promote controlled plastic hinge relocation away from the beam–column interface. This detailing can mitigate the pronounced EVDR reduction associated with extended flange-bonded configurations (e.g., L_f = $2h_b$), which, in the present study, compromised cyclic endurance under resonant excitation. Furthermore, given the high sensitivity of retrofit performance to excitation frequency, an effective retrofit design approach must jointly consider both the CFRP detailing system and the targeted excitation frequency to ensure optimized energy dissipation, controlled force demand, and improved cyclic durability.

It is important to acknowledge that the present analysis was limited to the fundamental vibration mode, a single structural configuration, and specific CFRP retrofit layouts, with all observed failure modes governed by ductile beam mechanisms. Future investigations should therefore extend this framework by incorporating higher-mode contributions and assessing the influence of ground motion records with broad frequency content on the EVDR of FRP-retrofitted systems. In addition, studies exploring a broader range of structural typologies, alternative CFRP layouts, and diverse failure modes (such as column-dominated mechanisms and joint shear degradation) would contribute to a more comprehensive and generalized seismic performance assessment. Such investigations would clarify how energy dissipation patterns evolve across distinct damage states, ultimately supporting seismic design approaches that more effectively integrate strength enhancement with energy-dissipation objectives in CFRP retrofit applications.

References

[1] ACI Committee 440.2R-17. Guide for the design and construction of externally bonded FRP systems for strengthening concrete structures, American Concrete Institute, Farmington Hills, Michigan, USA, 2017.

[2] Zarandi S, Maheri MR. Seismic performance of RC frames retrofitted by FRP at joints using a flange-bonded scheme. Iranian Journal of Science and Technology, Transactions of Civil Engineering. 2015;39(C1):103-123.

[3] Antonopoulos CP, Triantafillou TC. Experimental investigation of FRP-strengthened RC beam-column joints. Journal of Composites for Construction. 2003;7(1):39-49. https://doi.org/10.1061/(asce)1090-0268(2003)7:1(39)

[4] Arowojolu O, Ibrahim A, Rahman MK, Al-Osta M, Al-Gadhib AH. Plastic hinge relocation in reinforced concrete beam–column joint using carbon fiber–reinforced polymer. Advances in Structural Engineering. 2019;22(14), 2951–2965. https://doi.org/10.1177/1369433219855901

[5] International Federation for Structural Concrete (fib). Externally applied FRP reinforcement for concrete structures. fib Bulletin no.90, Lausanne, Switzerland, 2019. https://doi.org/10.35789/fib.bull.0090

[6] CNR-Advisory Committee on Technical Recommendations for Construction. Guide for the design and construction of externally bonded FRP systems for strengthening existing structures, Rome, Italy, 2004.

[7] Mahini SS, Ronagh HR. Web-bonded FRPs for relocation of plastic hinges away from the column face in exterior RC joints. Composite Structures. 2011;93(10):2460-2472. https://doi.org/10.1016/j.compstruct.2011.04.002

[8] Paulay T, Priestley MJN. Seismic design of reinforced concrete and masonry buildings, John Wiley & Sons, New York, USA, 1992.

[9] Hejazi F, Azarm R, Firoozi AA. Efficiency of flange-bonded CFRP sheets in relocation of plastic hinge in RC beam–column joints. Applied Sciences. 2023;13(21):11870. https://doi.org/10.3390/app132111870

[10] FEMA 356. Prestandard and commentary for the seismic rehabilitation of buildings, Federal Emergency Management Agency, Washington, D.C., USA, 2000.

[11] ATC. Seismic evaluation and retrofit of concrete buildings, Rep. No. ATC-40, Applied Technology Council, Redwood City, California, USA, 1996.

[12] Shaikh ZK, Sohoni VS. Efficacy of carbon fibre reinforced polymer (CFRP) laminates in retrofitting the damaged moment resisting RC frames. Discover Civil Engineering. 2025;2(1):166. https://doi.org/10.1007/s44290-025-00326-5

[13] Sakr MA, Seleemah AA, Khalifa TM, El-Samak G. Studying behavior of exterior RC beam–column joints strengthened using CFRP for achieving "strong column–weak beam" in RC frames. East African Scholars Journal of Engineering and Computer Sciences. 2019;2(2):53–68.

[14] Wang L, Xuan W, Zhang Y, Cong S, Liu F, Gao Q, Chen H. Experimental and numerical research on seismic performance of earthquake-damaged RC frame strengthened with CFRP sheets. Advances in Materials Science and Engineering. 2016;6716329. https://doi.org/10.1155/2016/6716329
[15] Wang Y, Chen W, Li D, Xu H, Zhang F, Guo X. Experimental and numerical investigations of the seismic performance of reinforced concrete frames strengthened with CFRP sheets. Buildings. 2023;13(9):2195. https://doi.org/10.3390/buildings13092195
[16] Zhou Y, Liu X, Zhang X, Guo X. Investigation on seismic performance of reinforced concrete frame retrofitted by carbon fiber-reinforced polymer. Buildings. 2024;14(6):1604. https://doi.org/10.3390/buildings14061604
[17] Pohoryles DA, Minas S, Melo J, Bournas DA, Varum H, Rossetto T. A novel FRP retrofit solution for improved local and global seismic performance of RC buildings: Development of fragility curves and comparative cost-benefit analyses. Journal of Earthquake Engineering. 2024;28(7):1914-1932. https://doi.org/10.1080/13632469.2023.2256891
[18] Eslami A, Dalalbashi A, Ronagh HR. On the effect of plastic hinge relocation in RC buildings using CFRP. Composites Part B: Engineering. 2013;52:350-361. https://doi.org/10.1016/j.compositesb.2013.04.025
[19] Ronagh HR, Eslami A. Flexural retrofitting of RC buildings using GFRP/CFRP–A comparative study. Composites Part B: Engineering. 2013;46:188-196. https://doi.org/10.1016/j.compositesb.2012.09.072.
[20] Balsamo A, Colombo A, Manfredi G, Negro P, Prota A. Seismic behavior of a full-scale RC frame repaired using CFRP laminates. Engineering Structures. 2005;27(5):769-780. https://doi.org/10.1016/j.engstruct.2005.01.002
[21] Le-Trung K, Lee K, Shin M, Lee J. Analytical assessment and modeling of RC beam-column connections strengthened with CFRP composites. Composites Part B: Engineering. 2011;42(7):1786–1798. https://doi.org/10.1016/j.compositesb.2011.07.002
[22] Abaqus Analysis User's Manual. Abaqus, 2017.
[23] Valles RE, Reinhorn AM, Kunnath SK, Li C, Madan A. IDARC2D, Version 4.0: A computer program for the inelastic damage analysis of buildings, National Center for Earthquake Engineering Research (NCEER), Technical Report NCEER-96-0010, New York, USA, 1996.
[24] Chopra AK. Dynamics of structures: theory and applications to earthquake engineering, 4th edition, Pearson, Boston, Massachusetts, USA, 2014.
[25] Carlos IA, Manuel SHJ, Ivan MD, Higinio GPJ. Energy balance analysis in non linear dynamic equivalent systems. MATEC Web of Conferences, 2018;148:03002. https://doi.org/10.1051/matecconf/201814803002
[26] Heitz T, Giry C, Richard B, Ragueneau F. Identification of an equivalent viscous damping function depending on engineering demand parameters. Engineering Structures. 2019;188:637-649. https://doi.org/10.1016/j.engstruct.2019.03.058
[27] Jacobsen LS. Damping in composite structures. Proceedings of the 2nd World Conference on Earthquake Engineering, Tokyo, Japan, 1029-1044, 1960.
[28] Rodrigues H, Varum H, Arêde A, Costa A. A comparative analysis of energy dissipation and equivalent viscous damping of RC columns subjected to uniaxial and biaxial loading. Engineering Structures. 2012;35:149-164. https://doi.org/10.1016/j.engstruct.2011.11.014
[29] Priestley MJN, Grant DN. Viscous damping in seismic design and analysis. Journal of Earthquake Engineering. 2005;9(sup2):229-255. https://doi.org/10.1142/s1363246905002365
[30] Priestley MJN, Grant DN, Blandon CA. Direct displacement-based seismic design. New Zealand Society for Earthquake Engineering (NZSEE) conference, 2005.
[31] Priestley MJN, Calvi GM, Kowalsky MJ. Direct displacement-based seismic design of structures. New Zealand Society for Earthquake Engineering (NZSEE) conference, 2007.
[32] Peng C, Guner S. Direct displacement-based seismic assessment of concrete frames. Computers and Concrete. 2018;21(4):355-365. https://doi.org/10.12989/cac.2018.21.4.355
[33] Hafezolghorani M, Hejazi F, Vaghei R, Jaafar MS Bin, Karimzade K. Simplified damage plasticity model for concrete. Structural Engineering International. 2017;27(1):68–78. https://doi.org/10.2749/101686616x1081
[34] Cornelissen HAW, Hordijk DA, Reinhardt HW. Experimental determination of crack softening characteristics of normal-weight and lightweight concrete. Heron Journal. 1986;31(2):45-56.
[35] MC90. CEB-FIP Model Code 1990, Bulletin d'Information No. 213/214, Comité Euro-International Du Béton, Thomas Telford, Lausanne, Switzerland, 1993.
[36] Sinha BP, Gerstle KH, Tulin LG. Stress-strain relations for concrete under cyclic loading. ACI Journal Proceedings. 1964;61(2):195-212. https://doi.org/10.14359/7775
[37] Nguyen NH, Whittaker AS. Numerical modelling of steel-plate concrete composite shear walls. Engineering Structures. 2017;150:1-11. https://doi.org/10.1016/j.engstruct.2017.06.030
[38] Lu J, Mou T, Wang C, Huang H, Han W. Research on hysteretic behavior of FRP-confined concrete core-encased rebar. Polymers. 2023;15(12):2728. https://doi.org/10.3390/polym15122728

[39] Shi K, Gao Z. Experimental and numerical study on flexural behavior of steel fiber reinforced high–strength concrete (SFRHC) beams. Scientific Reports. 2025;15:18338. https://doi.org/10.1038/s41598-025-02220-7

[40] Gulkan P, Sozen MA. Inelastic responses of reinforced concrete structure to earthquake motions. ACI Journal Proceedings. 1974;71(12):604-610. https://doi.org/10.14359/7110

[41] Akbaş B, Akşar B, Doran B, Alacalı S. Hysteretic energy to energy input ratio spectrum in nonlinear systems. Deu Muhendislik Fakultesi Fen ve Muhendislik. 2016;18(53):239-254. https://doi.org/10.21205/deufmd.20165318384

[42] White C. Resonance revealed: Understanding what really happens at resonance. Vibrations. 2018;35(1).